

Positron emission tomography in water resources and subsurface energy resources engineering research



Christopher Zahasky^{a,b,*}, Takeshi Kurotori^c, Ronny Pini^c, Sally M. Benson^a

^a Department of Energy Resources Engineering, Stanford University, Stanford, CA, United States

^b Department of Earth Science and Engineering, Imperial College London, London, England, United Kingdom

^c Department of Chemical Engineering, Imperial College London, London, England, United Kingdom

ARTICLE INFO

Keywords:

Positron emission tomography
X-ray computed tomography
Imaging
Solute mixing and spreading

ABSTRACT

Recent studies have demonstrated that positron emission tomography (PET) is a valuable tool for in-situ characterization of fluid transport in porous and fractured geologic media at the laboratory scale. While PET imaging is routinely used for clinical cancer diagnosis and preclinical medical research—and therefore imaging facilities are available at most research institutes—widespread adoption for applications in water resources and subsurface energy resources engineering have been limited by real and perceived challenges of working with this technique. In this study we discuss and address these challenges, and provide detailed analysis highlighting how positron emission tomography can complement and improve laboratory characterization of different subsurface fluid transport problems. The physics of PET are reviewed to provide a fundamental understanding of the sources of noise, resolution limits, and safety considerations. We then layout the methodology required to perform laboratory experiments imaged with PET, including a new protocol for radioactivity dosing optimization for imaging in geologic materials. Signal-to-noise and sensitivity analysis comparisons between PET and clinical X-ray computed tomography are performed to highlight how PET data can complement more traditional characterization methods, particularly for solute transport problems. Finally, prior work is critically reviewed and discussed to provide a better understanding of the strengths and weakness of PET and how to best utilize PET-derived data for future studies.

1. Introduction

The migration of contaminants in soils, the spreading and trapping of CO₂ in geologic carbon storage operations, fluid advection through fractured geothermal reservoirs, and oil recovery from both conventional and unconventional reservoirs, are examples highlighting the importance of understanding flow and reactive transport in geologic media. Many of these processes are transient and highly spatially localized. As a result, the development of techniques that can observe phenomena in-situ under representative conditions is highly valuable. The ability to measure the temporal and spatial evolution of the concentration of solutes, and to quantify rock and transport properties directly, provides not only a verification of our understanding of reactive transport in complex porous media, but additional insight for the engineering design of these subsurface processes.

The three main imaging technologies employed for continuum-scale fluid transport and fluid distribution characterization are clinical computed tomography (X-ray CT), nuclear magnetic resonance and imaging (NMR/MRI), and emission tomography (ET). X-ray CT is by far the

most widely used in Earth science applications and relies on the generation, transmission, and detection of X-rays through geologic materials. The measured spatial variation in X-ray attenuation reflects the variability in material and fluid electron density, which can be used to determine three-dimensional maps of porosity and fluid saturations (Akin and Kovscek, 2003). While micro-X-ray computed tomography has also gained widespread utilization in recent years (Blunt et al., 2013), it is largely used for observations of pore-scale processes on relatively small samples and will therefore be omitted from further discussion and comparison with continuum-scale imaging techniques. Magnetic resonance relies on measuring the response and re-equilibration of nuclear spins in a material when subjected to a strong magnetic field. Because this response depends on both fluid and rock properties, this imaging technique enables the mapping of flow and internal structure properties of a porous sample in multiple dimensions. NMR is commonly used during well logging to measure fluid saturation and porosity as a function of depth; these data are used to draw correlations with higher quality laboratory observations of the same properties (Mitchell et al., 2013). However, the presence of paramagnetic minerals in many

* Corresponding author at: Department of Earth Science and Engineering, Imperial College London, London, England, United Kingdom.
E-mail address: c.zahasky@imperial.ac.uk (C. Zahasky).

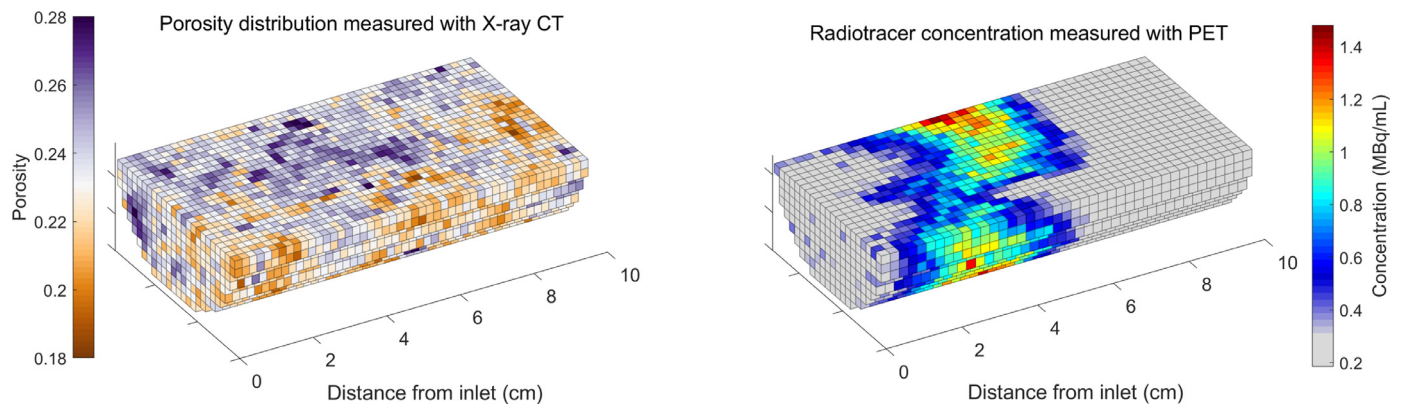


Fig. 1. (left) Porosity distribution of a 5 cm diameter Ketton limestone core measured with X-ray CT (Akin and Kovscek, 2003). (right) Reconstructed PET image illustrating the distribution of radiotracer concentration for a 2 mL pulse of tracer injected in the same Ketton limestone core. The tracer was injected at 4 mL/min and immediately displaced by water at the same rate. Tracer distributions are able to be measured with a temporal resolution as short as 10 seconds. The voxel size in the images above are roughly 12 mm³. The preclinical PET image was collected with the experimental system described in the Supplemental Information under ambient pore pressure and temperature conditions.

geologic materials can limit the application of MRI imaging in geologic porous and fractured media (Nestle et al., 2003; Reeves and Chudek, 2001; Werth et al., 2010). Emission tomography includes two main imaging techniques, positron emission tomography (PET) and single-photon emission computed tomography (SPECT), that rely on photon emission for in situ imaging. Positron emission tomography is the most common these emission tomography methods and will be the focus of this study. PET relies on the emission and detection of photons from positron-emitting radiotracers using cylindrical arrays of scintillation crystals. Tomographic reconstruction methods are used to obtain three-dimensional images of radiotracer distribution in the porous material as a function of time. Similarly to X-ray CT and MRI, PET has been developed for medical purposes, but is increasingly being used for applications in engineering and Earth science (Brattekas and Seright, 2017; Ferno et al., 2015b; Kulenkampff et al., 2018; Pini et al., 2016; Zahasky et al., 2018; Thorpe et al., 2019).

The distinct physics that underlie these imaging techniques determine their strengths and weaknesses for various applications in water resources and subsurface energy resources engineering. While X-ray computed tomography has become ubiquitous in geoscience experimental applications (e.g. porosity distribution measurements shown in Fig. 1), PET imaging has had limited utilization due to both real and perceived challenges of handling, injecting, and imaging radiotracers. However, the high spatial (millimeters) and temporal resolution (tens of seconds) available with PET imaging provides an unparalleled window into complex flow and transport processes at the core scale. An example highlighting the capabilities of PET for quantifying solute (i.e. radiotracer) transport in a strongly heterogeneous geologic porous media is illustrated in Fig. 1.

The aim of this study is to understand the unique capabilities of PET imaging for geoscience applications, to demonstrate and design protocols and procedures for successfully applying PET for rock imaging, and to determine the conditions under which PET provides advantages over other imaging techniques. In Section 2 the underlying physics of positron emission tomography will be described. This will provide a foundation for explaining the sources of error and both the theoretical and practical resolution limits of various PET imaging platforms that are described in the remainder of Section 2. In Section 3 the experimental design aspects of PET studies are discussed, including radiotracer selection and radiotracer handling safety, and new methods for performing PET imaging experiments with geologic materials are described. In the final section we provide examples and discuss the benefits and limitations of PET for different problems in porous and fractured media. We identify in-situ quantification of solute mixing, spreading, and diffusion;

sub-sample transport parameter (e.g. porosity and permeability) inversion; and fluid flow path identification and visualization as areas where PET imaging is providing information that is improving our understanding of transport in geologic media. However, with increasing adoption of PET imaging, there is a growing list of opportunities for future applications.

2. Review of PET imaging theory

During a PET scan positrons (e^+) are emitted as a result of the radioactive decay process of positron-emitting radionuclides (Eq. (1) for the case of an ^{18}F radionuclide). The positron decay also emits a neutrino (ν_e). As the positrons travel through the surrounding material they lose energy and slow down. When the positron has slowed down sufficiently, it can combine with an electron (e^-) and an annihilation event occurs. The distance travelled by the positron between radionuclide emission and annihilation is referred to as positron range, and can be as large as several millimeters.

As illustrated in the upper left of Fig. 2, this positron annihilation event produces two photons (γ) emitted in nearly opposite directions—due to conservation of momentum—each with an energy of 511 keV (Eq. (2)). The photon energy produced during positron-electron annihilation is described by the Special Theory of Relativity ($E = mc^2$), with m equal to the electron rest mass (Bailey et al., 2005).



These pairs of coincident photons are then detected with a three-dimensional array of photon detectors in the PET scanner. The entire three-dimensional volume of the sample is imaged simultaneously. In a PET scanner this array of detectors is commonly composed of individual inorganic scintillator crystals that emit visible light after being struck by a high-energy photon. A ‘coincidence event’ is recorded if the time between the detection of two photons at two different detectors is less than the defined coincidence time threshold ($\mathcal{O}(1)$ nanoseconds). In other words, two photons must strike different detectors within a specified time (coincidence time) to register a coincidence detection event. The line connecting the detectors excited during the coincident event is termed the line-of-response (LOR). However, because the photon detectors have a finite surface area, it is more accurate to conceptualize the volume between them as a parallelepiped, and to refer to it as the volume-of-response (VOR) (Kinahan et al., 2004).

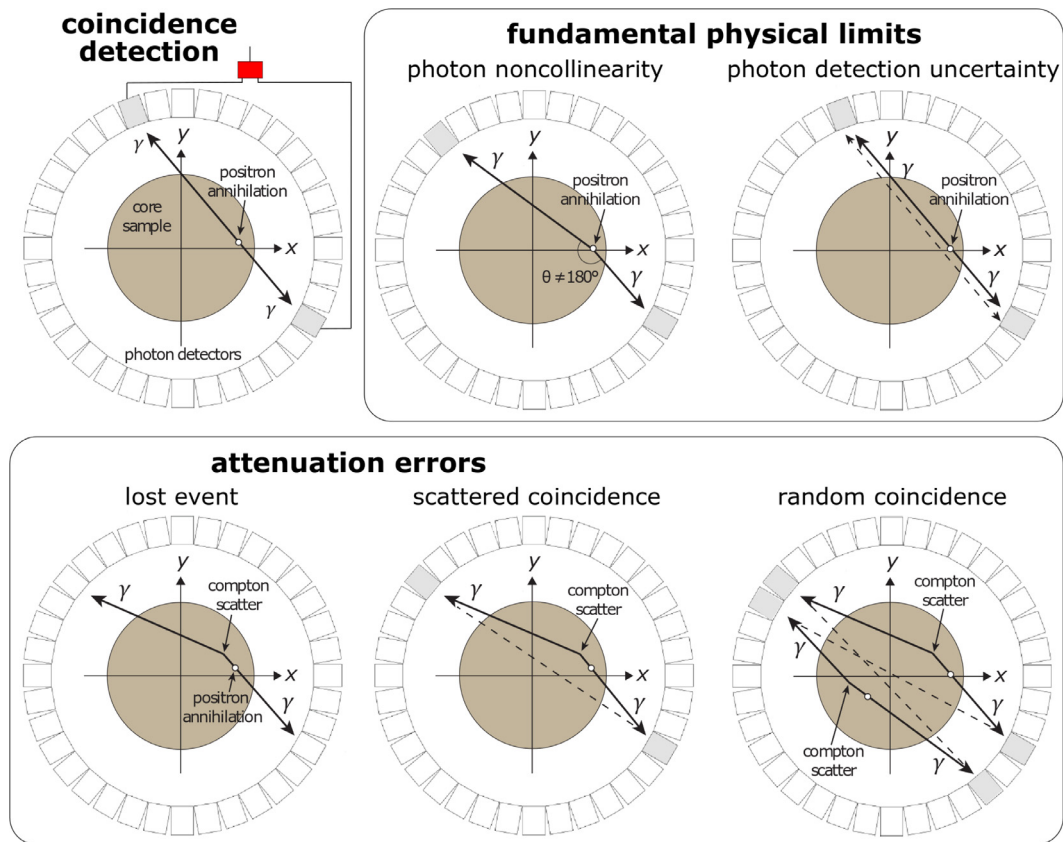


Fig. 2. (upper left) Illustration of unattenuated photon geometry and coincidence detection (with struck detector highlighted grey). (upper center) Illustration of photon noncollinearity. Line-of-response calculations assume that $\theta = 180^\circ$. (upper right) Photon detectors can not distinguish between photon paths described by the solid line versus a path described by the dashed line. (lower left) Lost event occurs when the difference between photon detection times at the photon detectors is greater than the coincidence time threshold. (lower center) Illustration of a scattered coincidence event. The dashed line indicates the false line of response determined for such an event. (lower right) Illustration of a random coincidence event. The dashed lines indicate two false LOR determined from separate annihilation events.

The random nature of positron emission, annihilation, and photon detection follows a Poisson probability distribution (Wernick and Aarsvold, 2004). The number of photons detected per second is described by the expectation operator E (Eq. (3)). Where $s(\mathbf{r})$ is the detection sensitivity in the parallelepiped at $\mathbf{r} = (x, y, z)$, and $f(\mathbf{r})$ is the three-dimensional distribution of tracer in the material being imaged (Kinahan et al., 2004).

$$E = \iiint_{VOR} s(\mathbf{r}) f(\mathbf{r}) d(\mathbf{r}) \quad (3)$$

The process of image reconstruction—converting a datafile of coincidence events to three-dimensional timelapse images—is an inverse problem where the tracer distribution, $f(\mathbf{r})$, is recovered. Once the raw coincidence events have been collected and parameterized as a sinogram, the following steps are required for image reconstruction: (1) correct for random coincidences and dead-time, (2) apply attenuation correction, (3) apply detector normalization, and (4) run reconstruction algorithm (Bailey et al., 2005). Signal intensity decline resulting from radioactive decay is corrected for during the reconstruction process by scalar corrections defined by the half-life of the radioisotope used for the study (see Section 3.1 for additional details on radiotracer selection). The details of analytical and numerical image reconstruction are beyond the scope of this report and can be found in a number of references (e.g., Bailey et al. (2005); Defrise et al. (2003)).

2.1. Sources of error and uncertainty

To understand how to optimize experimental data quality from PET scans, it is important to understand the physical sources of error

and the influence of photon-material interaction. Photons emitted from positron-electron annihilation events interact with the surrounding material between the point of annihilation and the point of detection. This material interaction is known as attenuation. Errors that arise from photon attenuation include lost events, scattered coincidence events, and random coincidence events. A second category of errors exist that are related to the fundamental physics of positron annihilation and photon detection. Sources of these errors include photon noncollinearity, positron range, and photon detector element size. All of these errors contribute to the overall resolution and noise of reconstructed PET images.

2.1.1. Attenuation of photons

As photons travel through a material, atomic interactions between the material and the photons result in photon attenuation. The two dominant mechanisms of photon attenuation are photoelectric absorption and Compton scattering (Akin and Kovscek, 2003; Bailey et al., 2005). Photoelectric absorption occurs when a photon's entire energy is absorbed by an inner electron of an atom. This effect is important for low energy photons in the range of 50–100 keV, as is common in low-energy X-ray CT scans, but is usually negligible for the 511 keV photons produced by positron annihilation. Compton scattering occurs when a photon interacts with an outer electron of an atom, resulting in the photon losing energy and being deflected from its original trajectory. The deflection angle is proportional to the amount of energy lost by the photon (Bailey et al., 2005). This effect occurs most commonly in photons with energies up to 5–10 MeV and can influence over 70% of all detected photons during a given PET scan depending on the material density (Levin, 2005; Zakhnini et al., 2013).

Compton scatter has the potential to create a number of errors in determining the LOR for a given annihilation event. First, a lost event occurs when one or both of the photons emitted from an annihilation event are deflected such that the difference between detection times at the photon detectors is greater than the coincidence time threshold or if the photon energy loss falls below the photon energy detection threshold (350 keV in settings used in this study). No coincidence event is recorded for lost events (lower-left illustration in Fig. 2). Second, a scattered coincidence event occurs when one or both photons are deflected, but the coincidence event is recorded because the difference between detection times of the photon pair is less than the coincidence time threshold. However, because of the deflection of one or both of the photons, the radiotracer location (i.e. the location of positron annihilation) does not lie on the line-of-response, leading to errors in the reconstructed image (lower-center image in Fig. 2). Third, a random coincidence event occurs when two positrons annihilate at nearly the same time. Scatter of these photons can lead to detection of two coincidence events where one photon from the first event is coincident with one photon from the second event. As illustrated in the lower right drawing in Fig. 2, this type of photon attenuation can also lead to noise and errors in radiotracer location in the image reconstruction process. For quantitative estimations of the influence of photon attenuation on coincidence detection events in dense materials see Monte-Carlo simulation study by Zakhnini et al. (2013).

2.1.2. Spatial resolution

Spatial resolution is a description of the level of detail that is discernible in an image and is different from the voxel dimensions chosen to describe an image—a term feature more accurately described as image definition (Pinoli, 2014). The fundamental physical limits of PET image spatial resolution result from the physics of positron annihilation and detection. Positrons are emitted at from radionuclides in the radiotracer. The path that any single positron takes through the surrounding material is random, but the statistical distribution can be described based on the initial energy of the positron and the properties of the surrounding material (Levin and Hoffman, 1999). For example, the full width at half maximum (FWHM) positron range distribution of ^{18}F -derived positrons in water is 0.102 mm (Levin and Hoffman, 1999). This implies that, even with perfect reconstruction and no photon attenuation, the maximum resolution is roughly 0.1 mm. However, the positron range will decrease with increased surrounding material/fluid density.

Another error that arises during the positron annihilation process is photon noncollinearity. Photon noncollinearity occurs when the coincident photons do not travel exactly 180° from each other (Fig. 2, upper-center) because the kinetic energy of the positron is not zero at the time of positron-electron annihilation. The impact of photon noncollinearity on image quality increases with scanner diameter (80 cm for clinical PET scanners and 10–20 cm for preclinical PET scanners). Accordingly, the use of smaller diameter commercial scanners commonly used in small animal medical research cuts the fundamental system spatial resolution roughly in half (Levin and Hoffman, 1999).

The last fundamental source of error comes from the finite size of the photon detectors that controls the size of the VOR between two de-

tectors. Many possible coincident photon paths lie within a particular VOR, making them indistinguishable during photon detection (upper-right illustration in Fig. 2). Preclinical PET scanners are typically able to achieve higher resolution by using detector arrays with smaller detector crystal sizes. The combination of positron range, photon noncollinearity, and finite photon detector size determines the fundamental spatial resolution limits for PET. The specific spatial resolution for different scanners will be discussed in the next section.

Understanding the fundamental physical limits of PET imaging enables the estimation of the maximum possible resolution of different PET scanners based on the diameter of the ring of photon detectors (d), the size of the detector crystals (w), and the positron range (r) for a given radioisotope. Moses (2011) has quantified these effects and derived an expression for determining the minimal spatial resolution (described by the FWHM in mm), also known as the ultimate spatial resolution (Γ), where it is assumed that there is no loss in resolution due to photon attenuation.

$$\Gamma = \sqrt{(w/2)^2 + r^2 + (0.0022d)^2} \quad (4)$$

To account for and quantify the actual resolution of PET data it is valuable to conduct studies with phantoms—synthetic systems with known geometry and features. Examples of such experiments that we have conducted will be presented in detail in Section 4, with emphasis on geologic materials. In addition to phantom studies, numerical and statistical analysis specific to the scanner setup and material attenuation can be performed to accurately understand and potentially improve image resolution (Zakhnini et al., 2013).

3. Methodology for application of PET in water resources and subsurface energy resources engineering research

3.1. Radiotracer selection

PET relies on the artificial production of positron emitting radionuclides that replace or are combined with a chemical compound to create a radiotracer. Radionuclides and radiotracers are typically chosen based on desired half-life, cyclotron generation capabilities, and the chemical properties or possible geochemical interactions with the tracer fluid. Table 1 shows a list of radionuclides that have been used in PET imaging studies in Earth sciences. By far the most commonly used radionuclide is ^{18}F , usually attached to Fludeoxyglucose ($[^{18}\text{F}]\text{FDG}$). $[^{18}\text{F}]\text{FDG}$ is widely available because it is the most common clinical radiopharmaceutical used for tumor identification and cancer diagnosis. As a result, there are hundreds of commercial and research facilities around the United States from which to purchase $[^{18}\text{F}]\text{FDG}$. $[^{18}\text{F}]\text{FDG}$ has been shown in a number of studies to behave as a conservative tracer (Kurotori et al., 2018b), unlike more reactive compounds, such as aqueous sodium bicarbonate ($[^{11}\text{C}]\text{NaHCO}_3$) solutions, that are known to be potentially reactive in carbonate rocks.

In addition to availability, radioisotope half-life is an important factor for radiotracer selection. The half-life of commonly used radionuclides varies by orders of magnitude, from 20 min for ^{11}C to 2.6 years

Table 1
Radioisotopes used in Earth science applications.

Isotope	Half-Life [$t_{1/2}$]	Studies
^{11}C	20.4 mins	Ferno et al. (2015b); Pini et al. (2016)
^{18}F	110 mins	Khalili et al. (1998); Ogilvie et al. (2001); Thorpe et al. (2019); Boutchko et al. (2012); Goethals et al. (2009); Maucec et al. (2013) Kulenkampff et al. (2008); Kurotori et al. (2018b) Brattekas and Seright (2017); Brattekas et al. (2016); Hu et al. (2017) Vasco et al. (2018); Zahasky and Benson (2016, 2018); Zahasky et al. (2018)
^{68}Ga	67.7 mins	Degueldre et al. (1996); Maguire et al. (1997)
^{64}Cu	12.7 hrs	Gouze et al. (2003); Hoff et al. (1996); Loggia et al. (2004); Gründig et al. (2007); Kulenkampff et al. (2018)
^{55}Co	17.53 hrs	Goethals et al. (2009)
^{124}I	4.2 days	Kulenkampff et al. (2008); Ogilvie et al. (2001)
^{22}Na	2.6 yrs	Ferno et al. (2015a); Kulenkampff et al. (2015); Lippmann-Pipke et al. (2017)

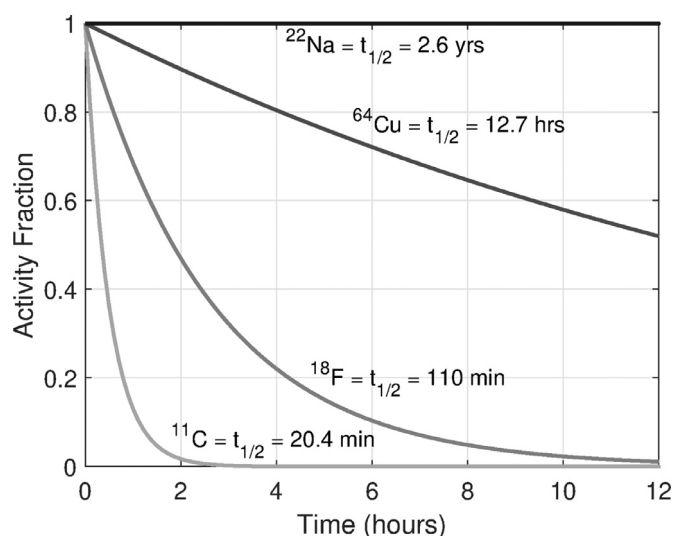


Fig. 3. Radioactive decay of common PET radioisotopes as a function of time.

for ^{22}Na , as illustrated in Fig. 3. Radioisotopes, such as ^{11}C and ^{18}F , work well for pulse injection experiments in high permeability samples (Brattekas and Seright, 2017; Pini et al., 2016; Zahasky and Benson, 2018). On the contrary, radioisotopes with longer half-life, such as ^{64}Cu or ^{22}Na , are well suited for experiments that analyze slower processes, such as diffusion or advection in low permeability samples (Hoff et al., 1996; Lippmann-Pipke et al., 2017).

One of the biggest advantages of using radiotracers is the range of fluids and carrier solutions that may be used, and the negligible influence of radiotracers on fluid characteristics such as viscosity and density. For example, in CT imaging high-density brine tracers are required to distinguish the tracer from the initial saturating fluid. As a result, strong gravitational effects may be observed in horizontal displacement experiments. To mitigate these effects the core-flooding system must be oriented vertically (Boon et al., 2016) or additional additives or salts must be added to the other fluids in the system to achieve buoyant neutrality (Kurotori et al., 2018b). For comparison, radiotracer solutions typically have a concentration up to 40 MBq/mL for preclinical PET imaging. With FDG having a molar mass of 181.1 g/mol, the corresponding FDG weight percent in solution is approximately $1 \times 10^{-9}\%$, while weight percent of NaI tracer is typically 5–10%. For more details see Section 2.1 of Kurotori et al. (2018b). The negligible impact of radiotracer on fluid properties enable experiments that more directly focus on the physics and chemistry of transport problems.

Although ^{11}C hydrocarbon gases have been used extensively for chemical engineering applications (Koriabkina et al., 2005; Noordhoek et al., 1998; Schumacher et al., 2000), only recently was radiotracer added to gas and compressed to a liquid phase to image transport in sandstone cores using PET with $[^{11}\text{C}]\text{CO}_2$ (Ferno et al., 2015b). Opportunities exist for developing radiotracers that are optimized for Earth science applications, especially those that can be added to aqueous solutions, gases, and non-aqueous phase liquids.

3.2. Radioactivity handling safety

The most important aspect of any experimental system is safety. While PET imaging studies present additional safety risks as compared with standard core-flooding experiments, the safety protocols are well developed and straightforward to implement. The main considerations for experiment safety are radioisotope half-life, radiotracer volatility and containability, radiotracer handling, automation and engineering controls, and system shielding. The radioisotope selection determines the amount of time that must pass before fluids may be disposed and

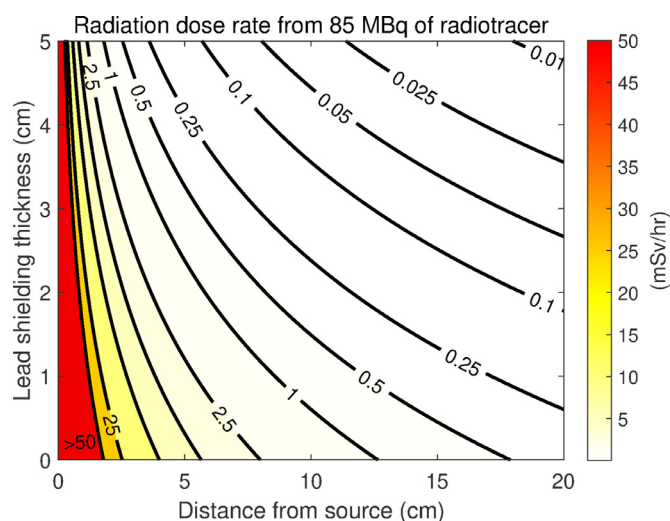


Fig. 4. Radiation exposure (millisieverts per hour) from 85 MBq of radiotracer as a function of distance from the radioactivity and lead shielding thickness ($\mu = 0.78 \text{ cm}^{-1}$). For reference, the often recommended annual dose limit for adults is 50 millisieverts (mSv) (dark red) and the typical organ dose from a single CT scan of an adult is approximately 20 mSv (Brenner and Hall, 2007). (For interpretation of the references to color in this figure legend, the reader is referred to the web version of this article.)

samples may be handled without radiation safety precautions. For typical activity levels used for PET imaging, this amount of time can be approximated as ten half-lives, corresponding to 3.4 h, 18 h, 5.3 days, and 26 years for ^{11}C , ^{18}F , ^{64}Cu , and ^{22}Na , respectively. As a result of this disposal criteria, it is beneficial to employ the radioisotope with the shortest half-life needed to obtain the desired measurements.

The three key aspects of radiation exposure reduction are minimizing exposure time, increasing distance from radioactivity, and proper radioactivity shielding. The presence of shielding decreases the fractional radiation intensity, $I_s/I_o = \exp(-\mu x_s)$, where I_s and I_o are the shielded and unshielded radiation intensity, respectively, μ is the linear attenuation coefficient for the shielding material, and x_s is its thickness. For example, one centimeter of lead around the pumps and other vessels containing radiotracer can cut the radiation exposure from 511 keV photons by more than 50%, two centimeters of lead will reduce exposure by 80%. Fig. 4 illustrates the reduction of radiation resulting from increased lead shielding thickness (y-axis) and increased distance from the radioactivity source (x-axis) across a range of values.

A number of system features may be added to reduce exposure time and increase distance from the system. Automating or building remote controls for pumps, switches, and other devices enables system control at large distances from the vessels and pumps containing radioactivity. Fig. 4 highlights the importance of increasing distance from a radioactive source for reducing radiation exposure. Having the system and controls set properly and practicing the experimental routine (i.e. ‘cold runs’) prior to handling and loading the radioactivity into pumps can reduce exposure time to the experiment operator.

Finally, all radioactivity handling facilities should have procedures, protocols, and practices dealing with minor and major spills. These protocols will vary depending on regulations, radioisotopes, and institutional resources. There are international rules and national laws for handling radioactivity. Work with PET requires trained personnel that is licensed to handle typical PET radionuclides with activity on the order of 10–500 MBq. The implementation of radiation exposure reduction methods in experimental system design and radioactivity handling practices, and proper safety protocols and procedures, significantly reduces the health and environmental risk of PET experiments.

3.3. Experimental design

To perform flow-through experiments imaged with positron emission tomography it is necessary to alter the experimental design of traditional flow-through or coreflooding systems (Alizadeh et al., 2014; Niu et al., 2015; Perrin and Benson, 2010) to safely handle, disposing, and quantify radiotracers. The additional components include custom sample holders, lead shielding, waste containers, additional pumps, switch valves, and radioactivity sensors. Emission tomography experiments have been performed in sample holders with a range of compositions including aluminum (Ferno et al., 2015b; Pini et al., 2016; Zahasky et al., 2018), polymers and plastics (Dogana et al., 2017; Maucec et al., 2013; Zahasky and Benson, 2018), and epoxy (Brattekas et al., 2016; Kulenkampff et al., 2015; Lippmann-Pipke et al., 2017). While low attenuation composites result in lower photon attenuation (Akin and Kovscek, 2003; Maucec et al., 2013), aluminum has been shown to be a cost-effective, durable option for range of emission and transmission imaging applications (Perrin and Benson, 2010; Zahasky and Benson, 2018). Dimensions of the sample holders is dependent/limited by the diameter of the scanner. As noted in Section 2.1.2, typical pre-clinical PET scanners have a diameter of 10–20 cm while clinical PET scanners have a typical diameter of 80 cm.

Shielding can be added in the form of lead bricks and lead machined to fit around experimental components such as the radioactivity detectors, tracer injection and back-pressure pumps, and the radioactivity waste reservoir. As described in Section 3.2, shielding is essential to reduce the radiation dose received by the experimenter and to reduce the background radiation that leads to noise during the PET scans and radioactivity sensor measurements.

In addition to the three-dimensional time-lapse imaging of the core, additional advantages of using radioactivity for solute transport studies include (1) the ease of acquisition of influent and effluent radioactivity concentrations, (2) higher probe signal-to-noise ratios, and (3) no inherent limitations on system pressures or temperatures. With simple, OEM scintillation detector probes housed in lead shielding it is possible to measure radioactivity concentration of fluid injected and produced from the sample. This information is useful not only for post-experiment solute transport analysis, but also for real-time information about the presence, concentration, and migration of radiotracer in the core-flooding system. This real-time radioactivity measurement is the only direct information about radiotracer transport available during PET imaging experiments, because reconstruction of the PET images can take hours and therefore may not be available until the experiments are completed. The ability to compare breakthrough curves from the outlet sensor with the three-dimensional data from PET imaging can be used to directly observe transport at multiple scales (e.g. spatially resolved inside the core and flux-weighted core averages at the outlet).

While the ultimate probe noise and resolution is dependent on a number of factors including the quality of the sensors, sensor measurement range, electronics configuration, and sensor calibration, with proper shielding the background measurement noise can be reduced to normal background levels. The sensitivity of the probes may be adjusted by changing the coil configuration of tubing around the sensors depending on the desired range of radioactivity concentrations used in the PET imaging experiments. With the proper configuration it is possible to measure concentrations up to four orders of magnitude smaller than the inlet concentration. This concentration range is often wider than is possible with brine or fluorescent tracers, which suffer from additional challenges such as pressure or chemical limitations (Vogler et al., 2018). This sensitivity is key for quantifying aspects of heterogeneity in natural systems such as long tailing in the breakthrough curves (Berkowitz et al., 2006).

The final benefit of using radiotracer for effluent analysis is that the radioactivity probes are not in direct contact with the fluids. The radiotracer flows through tubing coiled around the probes and emits photons that can easily pass through plastic, aluminum, and stainless

steel. As a result, there are no pressure, temperature, or fluid composition limitations with radioactivity probes. Conductivity probes typically require a flow cell to measure radioactivity that may be temperature dependent, limit experiment operating pressures, and introduce additional fluid dead volumes that can influence the solute transport analysis.

The system used for this study is very similar to the one described in Zahasky and Benson (2018) and is capable of continuous water and gas injection, PET imaging, radiotracer removal and shielding, and real-time data-logging of all of the experimental parameters, including inlet and outlet pressure, flow rate, and radiotracer concentration. Additional design specifications, radiotracer probe calibration, and a schematic and photograph of the experimental system are included in the Supplemental Information. Details of scanner and reconstruction settings used in this study can be found in Zahasky (2018).

3.4. Radioactivity dosing optimization

An essential parameter controlling shielding design, experiment safety, and optimal image quality is radioactivity dosing. Radioactivity dosing refers to determining the optimal level of radioactivity concentration for a given study without over-saturating the scanner with photons. Unlike biological and clinical applications of PET, in Earth sciences this optimum is often very near the maximum activity level that the scanner can record in order to acquire the highest data quality possible. In this section a new method is described to robustly and efficiently determine the proper radioactivity dosing for optimal image quality.

The maximum activity level that a particular PET scanner can quantify varies depending on the coincidence threshold setting, scanner geometry, photon detector size, photon detector dead-time (the crystal cool-down time before another photon may be detected), and scanner electronics. A practical way to determine this parameter is to start with a large dose of activity placed in a container similar in size to the anticipated spatial extent of radioactivity in the scanner during the experiments. In this study we filled a five centimeter diameter plastic bottle—a similar diameter as most of the cylindrical rock samples used in this study—with [¹⁸F]FDG diluted in water (123 mL). The initial activity of [¹⁸F]FDG (305 MBq) is measured with a dose calibration chamber and decays at a known rate (dotted black line in Fig. 5). With the activity in the scanner, repeated static scans of the radioactive phantom were acquired. Initially, the highly radioactive source is emitting positrons and generating more photons than the amount that the scanner can clearly differentiate, resulting in erroneous scanner radioactivity measurements (red symbols in Fig. 5). As the radioactive source decays, the measured scanner activity eventually corresponds with the known radioactivity of the phantom (blue symbols in Fig. 5). The location where these two lines intersect approximates the maximum radioactivity that can be imaged with a given PET scanner. This maximum radioactivity is independent of time-step length and histogram reconstruction settings.

Once the maximum radioactivity is known, the optimal radioactivity concentration of the tracer solution to be used in the experiments can be readily determined by dividing this radioactivity level by the volume of solution or the pore volume of sample, depending on the experimental methodology and objectives. The inset images in Fig. 5 illustrate pulses of radiotracer injected into a 8.9 cm diameter Berea core imaged under identical injection and scanner reconstruction settings. It is clear that the scan with a total radioactivity closer to the maximum has much lower noise than the scan with low activity. This type of optimization is essential for obtaining the highest quality data possible for quantitative analysis of radiotracer transport and distribution in geologic materials.

4. Quantitative assessment of image quality

4.1. Phantom studies for measuring spatial resolution

Once a radiotracer has been selected and an experimental system is built, it is valuable to quantify the spatial resolution of the PET

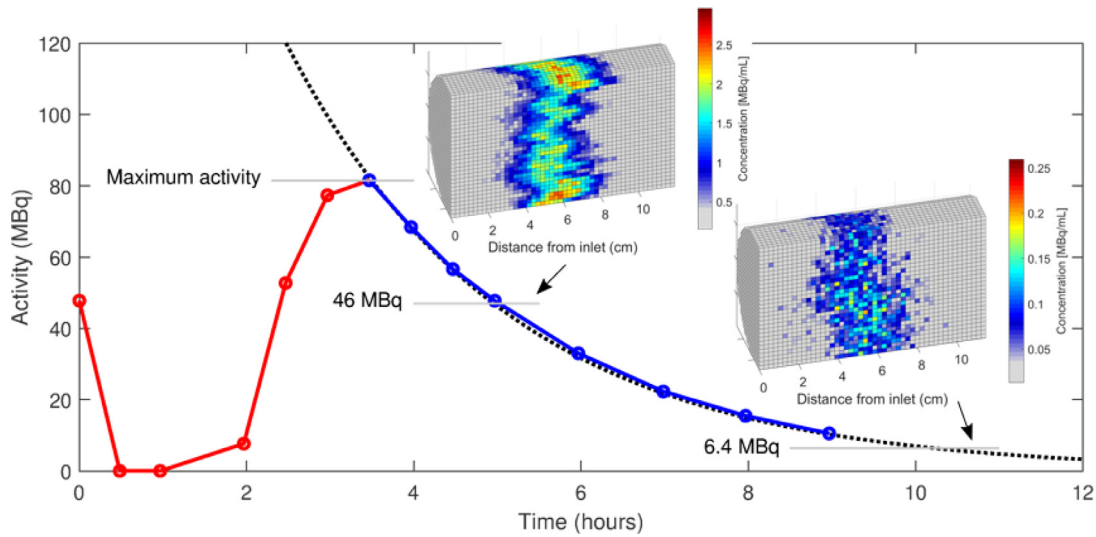


Fig. 5. Phantom radioactivity measured as a function of time with a Siemens Inveon preclinical PET scanner (colored points and solid line). The dashed black line indicates the known activity concentration based on dose chamber measurements of the radioactivity in the phantom. Note that at high concentrations the scanner fails to accurately measure the concentration due to detector element photon saturation. Inset images illustrate the tremendous improvement in image quality at near-optimal activity levels of a pulse of activity injected into a Berea sandstone core (activity levels indicated by horizontal grey lines). The inset images are acquired during dynamic tracer injection with a timestep length of two minutes (For interpretation of the references to color in this figure, the reader is referred to the web version of this article.).

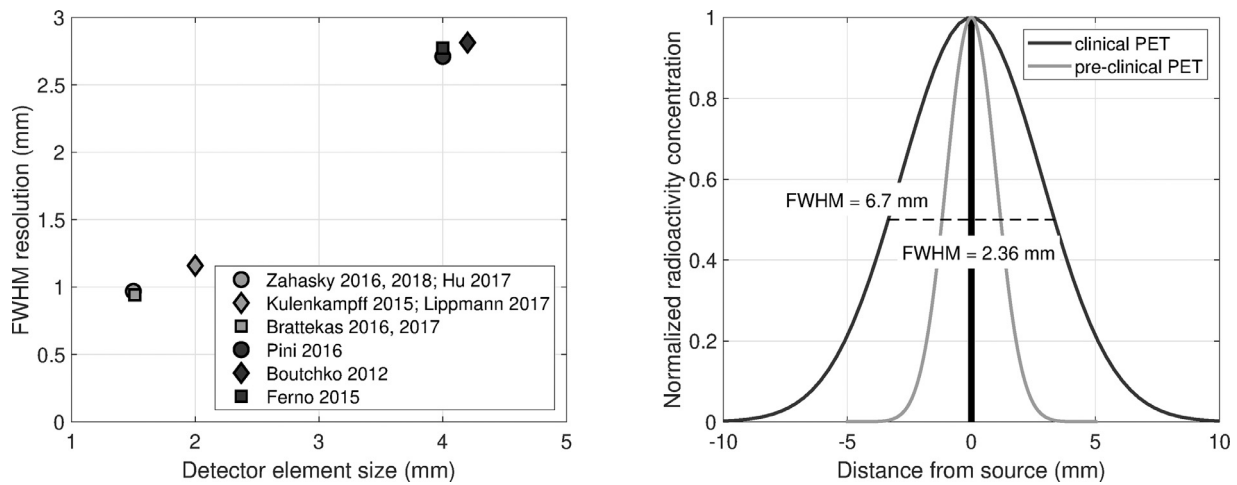


Fig. 6. (Left) Ultimate spatial resolution for different preclinical PET scanners (dark grey symbols) and clinical scanners (light grey symbols) used in imaging studies in Earth science. The resolution was calculated using the positron range of ^{18}F . (Right) The dark grey and light grey lines illustrate a Gaussian distribution function fit to the median normalized radioactivity concentration at increasing distances from the plane of a radiotracer imaged with a clinical PET scanner (dark grey circle in left plot) and preclinical PET scanner (light grey circle in left plot), respectively. The thickness of the vertical black line is equivalent to filter paper thickness ($\sim 200\ \mu\text{m}$). The horizontal dashed black line indicates the location of the FWHM measurements. The dark grey line is described by the function $\tilde{c}(x_p) = \exp(-(x_p/4.02)^2)$, the light grey line is described by the function $\tilde{c}(x_p) = \exp(-(x_p/1.42)^2)$. The Siemens Biograph PET data (red line) were reconstructed using the analytical Filtered Back Projection (FBP) algorithm (Defrise et al., 2003). The Siemens Inveon phantom data (blue line) were reconstructed with 3D Ordered Subset Expectation Maximization using Maximum A Priori (OSEM-OP MAP) (Hudson and Larkin, 1994).

imaging system for the desired application. Using Eq. (4) in Section 2.1.2 it is possible to estimate the ultimate resolution of a scanner based on its specifications. This value provides the maximum resolution possible neglecting losses arising from photon attenuation. However phantom studies with similar geometry, scanner settings, attenuation behavior, and radiotracer dosing account for the influence of photon-material interaction and reconstruction artifacts, and therefore provide a more accurate description of the expected image quality.

An example of experimental phantom analysis for determining the practical spatial resolution for planar feature identification, such as fractures, was performed using two different synthetic fracture-like features to create a planar source of radioactivity. The phantoms were imaged

with a Siemens Biograph 6 clinical PET/CT scanner and a Siemens Inveon preclinical PET scanner. The ultimate spatial resolution of the scanners is 2.8 mm and 1.0 mm, respectively, as estimated from Eq. (4) and shown in Fig. 6 (left plot, dark grey and light grey circles, respectively). Experimental method details and phantom designs are included in the Supplementary Information.

To quantify the resolution of the two imaging systems under experimental conditions, the measured radioactivity concentration is plotted at increasing distance from the plane of the radiotracer. Normalization of the radioactivity concentration ($\tilde{c}(x_p)$) further removes variation due to differences in radiotracer concentration across the filter paper and variations in radioactivity concentration due to radioactive decay.

Shown in Fig. 6 (right plot) are Gaussian functions fitted to the experimental data, for both the clinical PET (dark grey curve) and preclinical PET (light grey curve). The achieved spatial resolution of the instruments is quantified from the full width at half maximum (FWHM), which corresponds to the location where the measured concentration is equal to half of its maximum value. For the clinical PET, the latter corresponds to 6.7 mm, nearly double the ultimate spatial resolution (2.8 mm) estimated from Eq. (4), and more than double the preclinical PET FWHM resolution of 2.36 mm. This phantom example highlights the importance of phantom studies for resolution quantification, the improved resolution of preclinical PET scanners over clinical scanners, and illustrates a method for quantifying spatial resolution for fracture-based studies.

It is important to add that the preclinical PET scan was reconstructed with no attenuation correction. An attenuation correction map for the PET image reconstruction is often acquired with an X-ray CT scanner, or another low-energy photon transmission source, attached to the PET scanner. However, the Siemens Inveon CT scanner attached to the preclinical PET is designed for imaging small, low-density animals and therefore does not generate an X-ray beam with enough power to overcome the strong photoelectric adsorption that occurs in dense geologic materials. Future PET imaging systems designed exclusively for working with geologic materials could have higher power X-ray beams, similar to those used in clinical scanners (kV \approx 120, mA \approx 200) or micro-CT scanners for material science applications, that would enable PET-scan attenuation correction (Levin, 2005). CT-derived attenuation correction with reconstruction software developed and optimized specifically for high-density geomaterials has the potential to provide further improvement in image spatial resolution.

4.2. Feature identification and sensitivity

In addition to spatial resolution, imaging sensitivity and noise are important considerations (Gonzalez and Woods, 2017), particularly for

flow path identification and visualization. PET is particularly advantageous for small feature identification and characterization in centimeter-scale samples because it is able to provide high sensitivity, time-lapse spatial descriptions of fluid migration in heterogeneous systems. To quantify and demonstrate the sensitivity and benefits of PET imaging for fracture characterization specifically, we used a combination of measurements in geologic and synthetic fractures to calculate the signal-to-background ratio (SBR) of PET compared with clinical X-ray CT. Comparison with clinical X-ray CT is useful as this has traditionally been the most widely utilized imaging technique for tasks such as fracture aperture characterization (Bertels et al., 2001; Crandall et al., 2017; Huo and Benson, 2016; Huo et al., 2016; Ketcham et al., 2010; Watanabe et al., 2011; Wenning et al., 2018).

Signal-to-background measurements are subtly different from single-to-noise calculations because noise is defined as measurement variation only due to random scanner measurement errors. Alternatively, background noise is the combined effect of random scanner measurement errors and material variations (e.g. differences in porosity and mineralogy) that can mask a signal that is being measured. The signal-to-background ratio of X-ray CT for identifying small features will depend on both scanner imaging noise and geologic rock matrix attenuation variation (here described by attenuation standard deviation: σ_{matrix}). For example, in a homogeneous basalt, the matrix attenuation standard deviation is 60 Hounsfield units (HU) (solid blue line in Fig. 7). However, the matrix attenuation standard deviation in other geologic materials such as granitic rocks can be much higher due to coarse-grained mineralogical heterogeneity. The σ_{matrix} for a granite imaged with X-ray CT for this analysis was found to equal 200 HU (dashed blue line in Fig. 7). Similar matrix density variation may be produced by highly heterogeneous porosity fields.

When using PET to image and identify very small fractures in low porosity samples the background noise is only driven by random scanner noise. To quantitatively compare the signal-to-background ratio, the same fracture phantom described in Section 4.1 was filled with

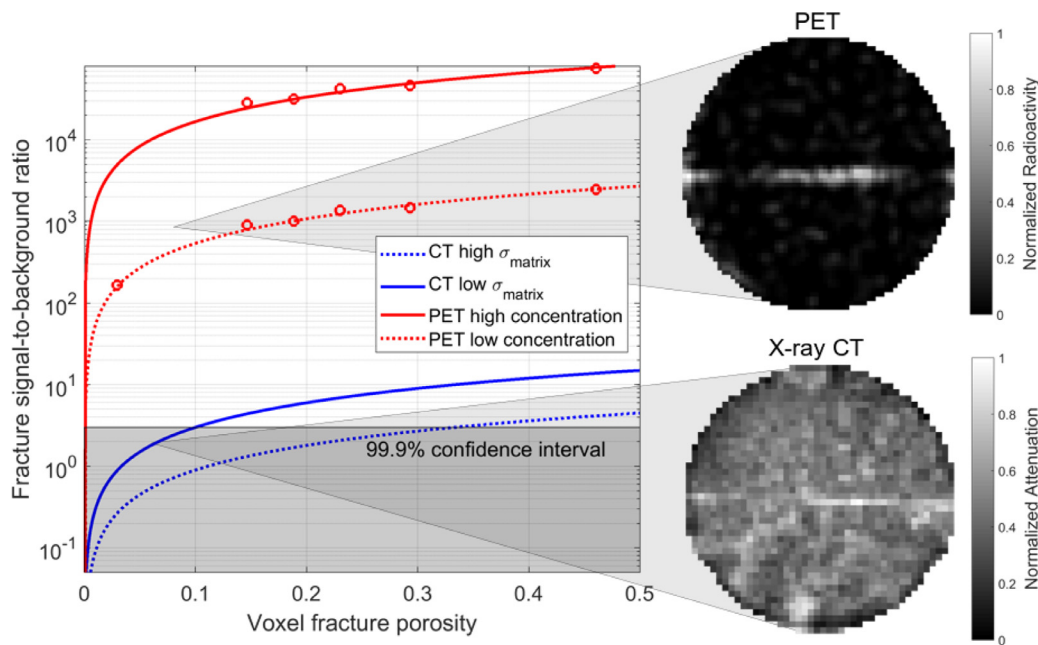


Fig. 7. Fracture signal-to-background ratio calculated using clinical X-ray CT in a basalt (low σ_{matrix}) and a granite (high σ_{matrix}) compared with the SBR of a planar feature imaged with a preclinical PET imaging systems. Fracture width (x-axis) is nondimensionalized by calculating the respective voxel porosity due only to the presence of fractures of different widths. The grey box indicates the upper limit of the 99.9% confidence interval above which a fracture can confidently be located. This threshold is determined by a SBR greater than five (Rose, 1974). The maps to the right qualitatively illustrate the signal produced by the presence of a planar saw-cut fracture in an otherwise homogeneous basalt core. The Hounsfield CT attenuation is normalized and traditional grey scale flipped (high attenuation areas are whiter) to enable visual comparison with normalized radiotracer concentration in the PET image. The normalization is performed with the calculation $CT_{norm} = (CT_{raw} - CT_{min}) / (CT_{max} - CT_{min})$, here CT_{raw} are the raw Hounsfield values, CT_{max} is the maximum raw Hounsfield value, and CT_{min} is the minimum raw Hounsfield value (For interpretation of the references to color in this figure, the reader is referred to the web version of this article.).

radiotracer and imaged with PET as the radiotracer concentration decayed. The calculated SBR at the high range of measurable radiotracer concentration with a preclinical scanner (72.15 MBq/mL) is shown by the solid red line in Fig. 7. The calculated SBR at a low radiotracer concentration (2.96 MBq/mL) is indicated by the red dashed line in Fig. 7.

To physically illustrate the SBR of a fracture imaged with PET in a geologic sample, a saw-cut homogeneous basalt core was injected with FDG radiotracer. The inset image in the upper-right of Fig. 7 shows the water-saturated fracture filled with radiotracer with a concentration of 20.35 MBq/mL. The basalt matrix porosity is effectively zero and the image is reconstructed with a voxel size of 0.78 mm \times 0.78 mm \times 0.8 mm. The lower-right inset image in Fig. 7 highlights the challenge of fracture identification in the same homogeneous basalt sample used for the PET imaging. The X-ray CT voxel size used for these calculations and the inset image is 1 mm \times 1 mm \times 1 mm. It is important to note that SBR will decrease with decreasing voxel size due to increasing random measurement error with smaller voxel dimensions (see Appendix A of Pini et al. (2012)).

From Fig. 7 it is clear that as the clinical CT matrix attenuation standard deviation increases it is more difficult to confidently identify the presence of a fracture and in low porosity samples PET imaging provides orders of magnitude better signal-to-background measurements. In samples with higher matrix porosity the imaging modality with a lower SBR will depend on sample porosity and porosity heterogeneity, matrix mineralogy, and minimum fracture aperture. Specific characterization of SBR will be necessary to understand the influence of these variations. However, accurate characterization is likely possible with a combination of CT and PET imaging methods. This analysis serves to highlight how PET is able to detect tracer concentrations in volumes orders of magnitude smaller than its spatial resolution, making it an ideal platform for fracture identification in geologic materials such as granites, basalts, and shales.

4.3. In-situ tracer imaging

In-situ imaging of radiotracers with PET also has a higher sensitivity and signal-to-noise ratio (SNR) than is possible with X-ray CT tracers. The temporal resolution of PET scans is higher than all but the most advanced clinical X-ray CT scanners and the required radiotracers concentrations are so small that changes in system fluid properties are often negligible. The most commonly used tracers for X-ray CT imaging are iodide salts such as potassium iodide (KI) or sodium iodide (NaI). Due to the high electron density of iodide, the enhanced X-ray attenuation enables it to be distinguished from other water or brine liquids in the

sample. As described in Section 3.1, the drawback of using brine solutions is the change in fluid density that results from the addition of the quantities of salt required to obtain a strong SNR.

To quantitatively compare the signal-to-noise behavior of clinical X-ray CT and preclinical PET imaging, pulse injection experiments with both saline tracers and radiotracers were performed. Short (2 mL) pulses of tracer were injected into a 5 cm diameter Bentheimer sandstone sample using the same procedure described in previous studies (Kurotori et al., 2018b; Zahasky and Benson, 2018) with the core-flooding system described in the Supplemental Information. For X-ray CT imaging, aqueous solutions of KI (6.06 wt%) and KCl (7 wt%) were used as tracer and carrier fluid, respectively, injected at a flow rate of 1 mL/min. X-ray CT scans were acquired every 4–5 min and the concentration of tracer was measured by subtracting baseline scans of the core fully saturated with KCl from scans with the KI pulse traveling through the core. For PET imaging, [18 F]FDG (21.13 MBq/mL) and water were used as tracer and carrier fluid, respectively, injected at a flow rate of 2 mL/min. The PET scans were reconstructed with time-steps of 95 seconds. A qualitative comparison of three-dimensional voxel concentrations is shown in Fig. 8 after approximately 0.4 pore volumes of carrier fluid were injected into the sample. Both the spatial structure of the tracer plume and the tracer distribution within the plume are more clearly resolved in the PET images as compared to those acquired with the X-ray CT scanner.

A more quantitative comparison of the same dataset is shown in Fig. 9. The top plot illustrates the calculated SNR for PET and CT along the length of the sample. The maximum SNR in the PET profile is 184 while the maximum SNR in the CT profile is 3.25. In this case, the signal is the slice-averaged concentration and the noise is quantified by calculating the standard deviation of voxel concentration variation in all of the voxels in the regions of the core that contain no tracer. A region is determined to have no tracer if the slice-averaged concentration is less than 1% of the maximum slice-averaged concentration. The lower plots in Fig. 9 show axis-parallel concentration profiles (colored lines) and the standard deviation of concentration measurements (indicated by width of grey regions) for X-ray CT (middle plot) and PET (lower plot). It is important to emphasize that CT SNR is a function of material (i.e. KI brine) electron density contrast relative to other fluid in pore space (i.e. KCl brine), and therefore is independent of scan time. The PET SNR is a function of radioactivity concentration and to a lesser extent image timestep length (image quality was found to be consistent down timesteps as short as 10 seconds). Both the qualitative and quantitative comparison of the saline and radioactive tracers make it clear that the tracer imaged with PET has a higher sensitivity and

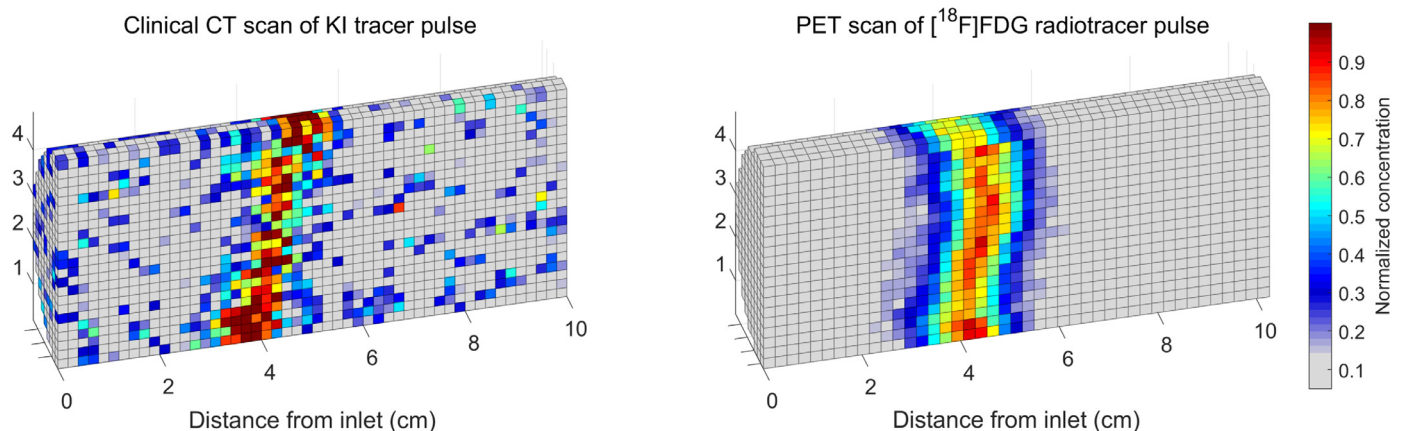


Fig. 8. Comparison of in-situ imaging of normalized radiotracer pulse and normalized high-density saline pulse in the same Bentheimer sandstone core imaged with preclinical PET and clinical X-ray CT respectively. The left plot is imaged with a Toshiba Aquilion 64 TSX-101A clinical X-ray CT scanner (voxel size: 2.02 mm \times 2.02 mm \times 2 mm) and the right plot is imaged with a Siemens Inveon preclinical PET (voxel size: 2.33 mm \times 2.33 mm \times 2.39 mm). Concentrations are normalized by dividing by the maximum slice-average concentration from the first scan or image of the respective experiments. Scans provide qualitative illustration of noise analysis described in detail in Fig. 9.

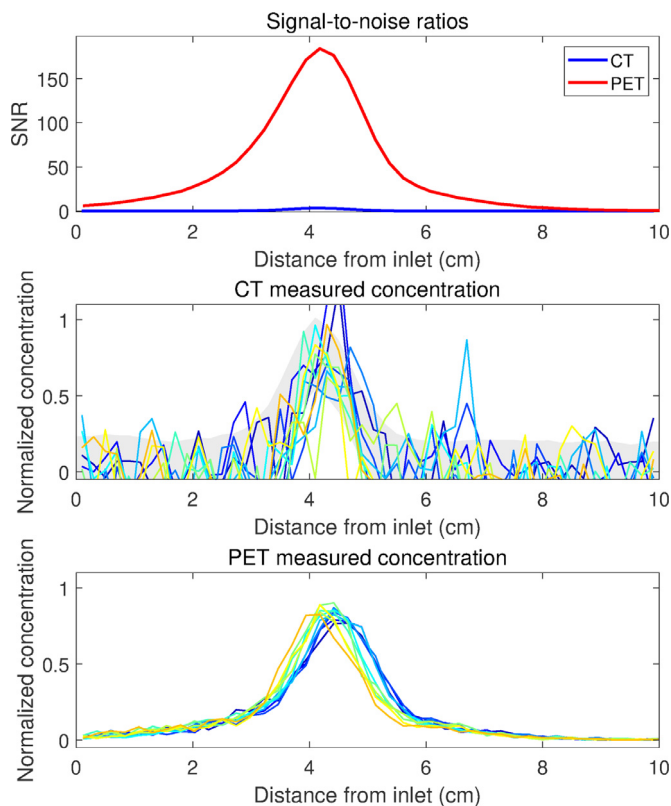


Fig. 9. (top) Comparison of signal-to-noise ratio of X-ray CT and PET measurements of a pulse of tracer in the same Bentheimer sandstone core. (middle) Axial-parallel normalized concentration profiles for 11 rows of voxels located along a horizontal slice of the core, measured with X-ray CT. Shaded grey region indicates measurement uncertainty as determined by the standard deviation of voxel concentrations containing no tracer. (bottom) Axial-parallel normalized radioactivity concentration profiles for 11 rows of voxels located along a horizontal slice through the center of the core, imaged with PET. Standard deviation of voxel concentrations is thinner than colored lines.

a much higher signal-to-noise ratio compared with X-ray CT imaging, making it well suited for studies on in-situ quantification of mixing and spreading.

5. Examples of applications in water resources and subsurface energy resources engineering

Positron emission tomography has been utilized for a number of applications in Earth science including measuring porosity, multiphase fluid saturation, dispersion, and diffusion in porous and fractured media as well as general fluid transport pathway identification and visualization. In the following section, these applications are reviewed and analyzed by presenting a selection of findings from studies reported in the literature.

5.1. In-situ quantification of solute mixing and spreading

A number of studies have used PET imaging to observe the transport of tracers in rocks and to quantify the underlying mechanisms, including hydrodynamic dispersion and diffusion. PET is ideally suited for solute advection and dispersion quantification in geologic materials due to the high sensitivity of radiotracer measurements, excellent temporal resolution, and negligible influence of radiotracer on fluid transport properties, as discussed in detail in Section 4.3. The in-house ClearPET scanner at the Helmholtz Center (HZDR, Germany) has been used to investigate the migration of radioisotopes in clay-rich rocks, including ^{22}Na (Lippmann-Pipke et al., 2017), ^{58}Co (Zakhnini et al., 2013), and

^{124}I (Kulenkampff et al., 2015, 2016). In these studies, direct observations of the molecular diffusion process were obtained over a range of length-scale (1–100 mm) and have enabled the quantification of diffusion anisotropy in these materials. In earlier work, this research group also combined observations using two different aqueous radiotracers (^{18}F]KF and ^{124}I]KI), enabling the quantification of transverse diffusion from fractures into the intact rock matrix (Kulenkampff et al., 2008). A similar experiment was conducted by Ferno et al. (2015b), although in this case liquid $^{11}\text{CO}_2$ at 10 MPa was used to measure diffusion from the gas-filled fracture into an oil-saturated Bentheimer sandstone matrix. The results of Ferno et al. (2015b) agree well with previously reported diffusion coefficients and confirm early achievements in the study of the diffusion of light hydrocarbons in porous materials using PET (Koriabkina et al., 2005; Noordhoek et al., 1998; Schumacher et al., 2000). In this context, while the short half-life of ^{11}C represents a challenge for diffusion measurements in geomaterials (i.e. Fig. 3), opportunities exist to develop new radiotracers for geo-specific applications such as those bound to geologically relevant contaminants or tracers soluble in different nonaqueous phase liquids.

A number of studies have exploited the high temporal resolution of emission tomography to study the advective mixing of tracers in geomaterials, including sandpacks (Boutchko et al., 2012), soils and glass beads (Dogan et al., 2017; Gründig et al., 2007; Perret et al., 2000; Richter, 2007; Vandehey et al., 2013), sandstones (Kurotori et al., 2018a; Pini et al., 2016; Zahasky and Benson, 2018) and carbonates (Kurotori et al., 2018a, 2018b). As an example of general validity, Fig. 10 illustrates the temporal evolution of a ^{18}F]FDG plume in a five-centimeter diameter, ten-centimeter long Edwards Brown carbonate rock core (Kurotori et al., 2018a). The strong subcore-scale heterogeneity present in the rock sample produce an evident distortion of the solute plume. Similar heterogeneous flow velocities were quantified in soil columns by Gründig et al. (2007) and Richter (2007). By providing direct access to the spatial structure of the concentration field within the plume, PET enables the quantification of mixing, spreading, and fluid-rock interaction over time and provides the means to relate it to the degree of structural heterogeneity of the porous medium (e.g. Fig. 1).

Emission tomography of solute transport can also be applied to geochemical and subsurface microbial transport studies to better understand fluid-rock interactions. Boutchko et al. (2012), Vandehey et al. (2012), Smith et al. (2017) and Dogan et al. (2017) have demonstrated that it is possible to not only image local structural heterogeneity, but also understand the influence of local system geochemistry or microbial conditions on ^{99}Tc transport in soils using SPECT and/or gamma camera imaging. Vandehey et al. (2012) was able to highlight these fluid-rock interactions by using ^{99}Tc in the form of ^{99m}Tc (VII) to understand geochemical immobilization potential in sediments before and after microbial stimulations, and then used the relatively common ^{99m}Tc -DTPA radiopharmaceutical as a conservative tracer to characterize non-reactive solute transport in the same soil systems. Thorpe et al. (2019) recently used PET to image and quantify the uptake of ^{18}F]FDG by indigenous microorganisms in packed sediment columns, demonstrating how future studies may employ PET to understand microbial metabolic and transport activity in the complex subsurface environments.

When coupled to a suitable numerical model, these experiments provide unique insight into the mechanisms of transport in heterogeneous porous media. Boutchko et al. (2012) used results from experimentally imaged pulse injections to build homogeneous simulations to measure core-averaged pore water velocity and porosity. Pini et al. (2016) applied the concept of streamtube analysis on the advection dispersion equation (ADE) to decouple the effects of spreading (originating from subcore permeability heterogeneity) from those of mixing (originating from pore-scale hydrodynamic dispersion). This analysis was expanded by Zahasky and Benson (2018) to measure subcore-scale dispersion during multiphase water-gas co-injection experiments in various sandstone cores. By applying the so-called Multi-Rate Mass

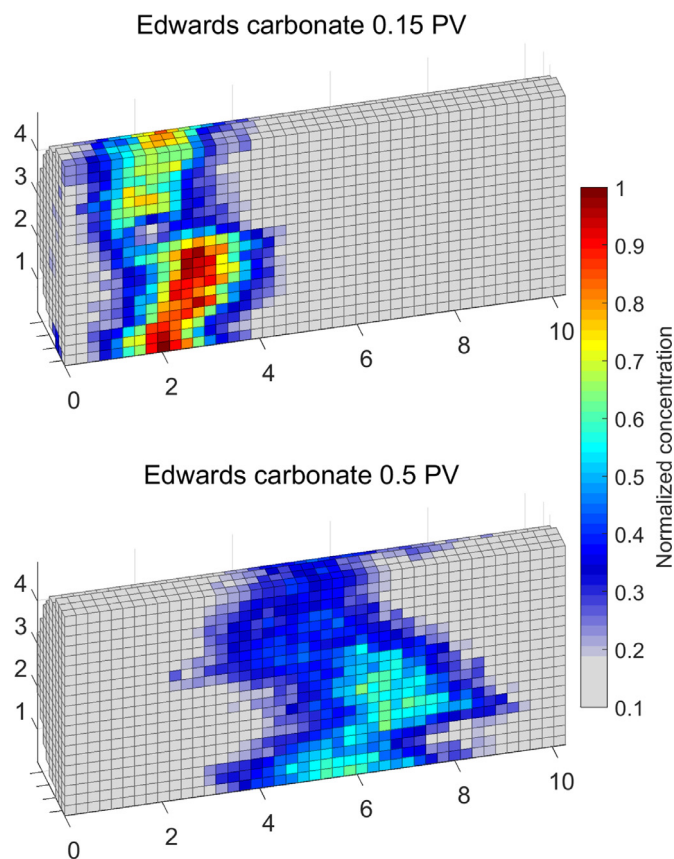


Fig. 10. Reconstructed PET images showing the distribution of normalized radiotracer concentration injected in an Edwards Brown carbonate. The tracer was injected at 2 mL/min and immediately displaced by water at the same rate. Tracer distributions are shown at two different times as described by pore volumes (PV) of water injected following tracer injection. Preclinical PET images were collected with the experimental system described in Section 3.3 under ambient pore pressure and temperature conditions.

Transfer (MRMT) model to breakthrough experiments in a microporous limestone Kurotori et al. (2018b) revealed the presence of mass transport limitations in the porous rock in the form of a characteristic flow-rate effect; the latter was attributed to the presence of micrometer-scale intra-granular porosity.

As evidenced by these examples, the analysis of dispersive flows in geomaterials is complicated by the presence multi-scale heterogeneities, which control the mixing process. While PET imaging provides the required information to advance our understanding of the underlying transport process, significant opportunities exist to work with radiochemists to develop tracers for analysis to displacements involving additional phenomena, such as adsorption, microbial transport, chemical reactions, and wettability/capillary effects.

5.2. Flow path identification and visualization

Numerous studies have utilized PET for flow path identification and visualization for a variety of different applications. Kulenkampff et al. (2008) used PET to investigate the flow through a fractured granite core, first demonstrating the ability of PET to accurately identify the location of fractures within geologic materials and to describe the complex flow topologies associated with these fractures. Imaging of high pressure fluid injection in fractures with PET was first demonstrated by Maucec et al. (2013). For the high-pressure injection Maucec et al. (2013) utilized a novel coreholder constructed from polyetherimide, an amorphous polymer composite, that had a pressure

rating up to 34 Mpa (~5000 psi) and reduced photon attenuation by a factor of eight relative to coreholders constructed from stainless steel.

Building on these demonstrations of PET imaging for static flow path identification, Brattekas et al. (2016) and Brattekas and Seright (2017) used PET to visualize dynamic changes in flow path geometry during dynamic polymer gel rupture and wormhole development in fractured carbonates. This in-situ imaging enabled descriptions of local blocking and fluid diversion capabilities of the polymer gel emplacement, complementing and helping explain flow conditions responsible for changes in bulk permeability and pressure behavior of the samples.

With multi-modal imaging, more quantitative discrete flow feature characterization is possible across a range of scales. Specifically, with X-ray computed tomography it is possible to characterize the rock, pore, and fracture structure of geologic materials down to the micrometer scale. PET imaging can then be used to quantify how fluid transport is influenced by these heterogeneous structures. Zahasky et al. (2018) demonstrated how preclinical PET, X-ray micro-CT, and clinical X-ray CT can be used to identify fluid flow pathways through vesicular basalt samples. The preclinical PET images were then registered with the micro-CT images to uniquely quantify connected pore space and effective surface area of the basalt samples. Multi-modal imaging strategies have tremendous potential to quantify different types of fluid transport mechanisms such as fluid flow in fractures, fracture-matrix-fluid interaction, and imbibition.

5.3. Multiphase fluid saturation measurements

The current methodology to measure in-situ fluid saturations with PET imaging relies on a linear relationship between the measured radiotracer activity and the local saturation (Ferno et al., 2015a; Zahasky and Benson, 2016). Validation of the linear scaling of radioactivity concentration and image intensity has been performed in phantom testing and is a necessary condition of the dosing optimization results described in Section 3.4. To calculate fluid saturation, the radiotracer in a given voxel must reach the known injected radiotracer concentration. This can be a major challenge in heterogeneous porous media where some pores experience very slow radiotracer advection (e.g. Figs. 1 and 10). If the voxels of interest are not fully saturated with radiotracer, the fluid saturation of the phase containing the radiotracer will be underestimated. The second major challenge is related to activity dosing described in Section 3.4 and to the trade-off between tracer concentration and image noise. On the one hand, the amount of tracer should be low enough to avoid saturating the scanner with high energy photons. This is particularly important for rock samples with large pore volumes and limits the maximum deployable tracer concentration (in a typical five centimeter diameter by ten centimeter long sandstone core the pore volume is often in excess of 20 mL). On the other hand, as the radioactivity concentration decreases, the voxel concentration measurement noise increases, thereby reducing the accuracy of the saturation measurement at the voxel scale. While these studies indicate that quantitative saturation measurements are possible with PET, methods developed to measure fluid saturations with clinical and industrial X-ray computed tomography (Akin and Kovscek, 2003) remain easier and typically more accurate.

5.4. Parameter inversion

One of the potentially most impactful applications of PET is for flow parameter characterization and testing transport inversion methods and models. Zahasky and Benson (2018) used preclinical PET to image pulses of [¹⁸F]FDG radiotracer injected during single phase and multiphase water-gas co-injection experiments in two different sized heterogeneous Berea sandstone cores. Using a streamtube approximation to reduce the spatial dimensions of the problem from 3D to 2D, spatial moment analysis of the preclinical PET data was used to measure

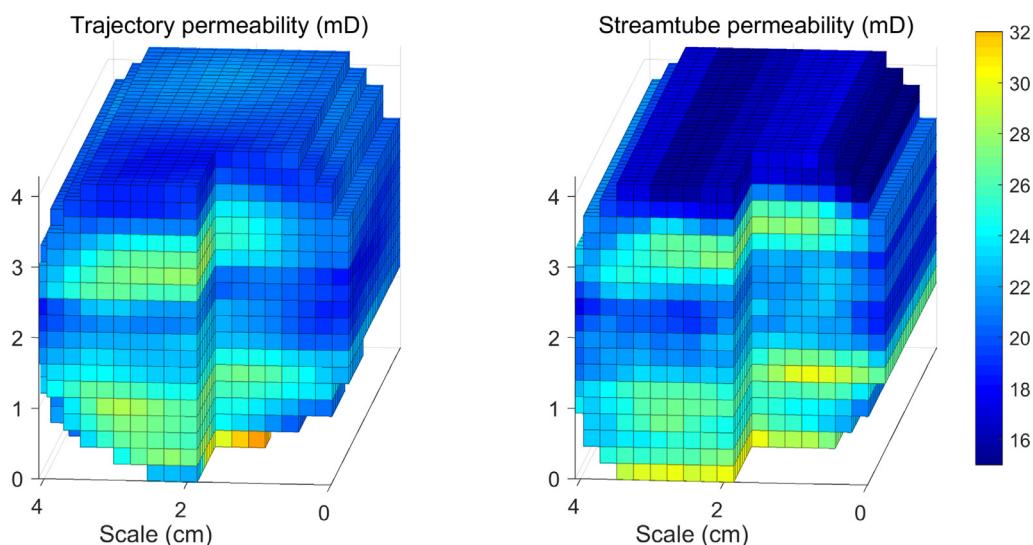


Fig. 11. Comparison of sub-core permeability distribution in heterogeneous Berea sandstone core evaluated using the trajectories method of Vasco et al. (2018) (left image) and the streamtubes method of Zahasky and Benson (2018) (right image).

the pore water velocity and flux of the radiotracer pulse in the aqueous phase. These measurements enabled sub-core calculations of porosity, permeability (right image in Fig. 11), water saturation, water relative permeability, and dispersivity. Vasco et al. (2018) expanded the inversion to three dimensions by using voxel mean arrival times and numerical simulation to determine fluid transport trajectories and calculate the three dimensional sub-core permeability field in the heterogeneous Berea core (left image in Fig. 11). There exist a growing number of possible methods from fields such as machine learning, optimization, and stochastic hydrology for inverting large datasets to determine sub-core permeability (e.g. Lee et al. (2016)) and relative permeability. Using preclinical PET data sets there is significant potential for future studies to test and develop new transport inversion and upscaling methods in heterogeneous geologic materials.

6. Conclusion

In-situ imaging will continue to help improve understanding of fluid transport mechanisms from the pore to the core scale, and provide essential data for building and testing models used to describe larger-scale transport problems. In this study we summarized the physics of PET imaging and how these physics along with photon-material interaction during data acquisition lead to the fundamental limits of image resolution. Methods of phantom analysis were described to efficiently characterize image resolution. Several PET experimental design considerations were discussed including radiotracer selection, a method for determining the optimal radioactivity concentrations, and important safety considerations. While these aspects introduce unique challenges to working with PET, this work is a guide to overcome these challenges.

Positron emission tomography has been used to study a range of problems from quantification of solute mixing and spreading, fluid saturation measurements, flow path identification, and parameter inversion. PET imaging is especially well suited for solute mixing and spreading quantification due to the high signal-to-noise ratio, excellent temporal resolution, and negligible influence of radiotracer on fluid transport properties. Analysis of solute pulse injection experiments indicate that with optimal radioactivity dosing PET has a signal-to-noise ratio over 50 times greater than that of clinical X-ray CT. We also analyzed data from PET scans reconstructed with timesteps as short as 10 seconds; these datasets showed negligible loss in data quality relative to longer reconstruction timestep sizes. Similarly, the sensitivity of PET imaging systems to the presence of radiotracer allows for even the smallest features

containing radioactivity to be identified as indicated by the fracture signal-to-background analysis. With detailed knowledge of the physics, current and ongoing experimental method development, and a clear understanding of benefits and limitations as described in this study, PET imaging techniques will be more fully utilized for challenging problems in water resources and subsurface energy resources engineering.

Acknowledgments

Work by Christopher Zahasky and Sally M. Benson was supported by the Global Climate Energy Project, the Stanford Center for Carbon Storage, and the Stanford Department of Energy Resources Engineering. The Inveon DPET (preclinical PET) scanner was funded by NIH grant number 1S10OD018130-01. The preclinical PET phantom study and fracture detectability analysis were funded by the U.S. Department of Energy (DOE), Office of Science, Office of Basic Energy Sciences (BES), Center for Mechanistic Control of Water-Hydrocarbon-Rock Interactions in Unconventional and Tight Oil Formations (CMC-UF) Award DESC0019165. The clinical CT tracer experiments were performed at Imperial College of London and carried out as part of the Qatar Carbonates and Carbon Storage Centre (QCCSRC), with funding provided jointly by Qatar Petroleum, Shell, and the Qatar Science and Technology Park. Nick Vandehey provided the data for the clinical PET phantom analysis. Nick Vandehey, James O'Neil, Tim Doyle and Frezghi Habte provided essential radioisotope handling training, PET scanner training, instruction, and advice. The authors thank the six anonymous reviewers for their careful review of the manuscript and their suggestions for improvements.

Supplementary material

Supplementary material associated with this article can be found, in the online version, at doi:10.1016/j.advwatres.2019.03.003.

References

- Akin, S., Kovscek, A., 2003. Computed tomography in petroleum engineering research. *Appl. X-ray Comput. Tomogr. Geosci.* 215, 23–38.
- Alizadeh, A.H., Khishvand, M., Ioannidis, M.A., Piri, M., 2014. Multi-scale experimental study of carbonated water injection: an effective process for mobilization and recovery of trapped oil. *Fuel* 132, 219–235. <https://doi.org/10.1016/j.fuel.2014.04.080>.
- Bailey, D.L., Townsend, D.W., Valk, P.E., Maisey, M.N. (Eds.), 2005. *Positron Emission Tomography*. Springer Science, London.

- Berkowitz, B., Cortis, A., Dentz, M., Scher, H., 2006. Modeling non-fickian transport in geological formations as a continuous time random walk. *Rev. Geophys.* 44 (RG2003). <https://doi.org/10.1029/2005RG000178.1>.
- Bertels, S.P., DiCarlo, D.A., Blunt, M.J., 2001. Measurement of aperture distribution, capillary pressure, relative permeability, and in situ saturation in a rock fracture using computed tomography scanning. *Water Resour. Res.* 37 (3), 649–662. <https://doi.org/10.1029/2000WR900316>.
- Blunt, M.J., Bijeljic, B., Dong, H., Gharbi, O., Iglauer, S., Mostaghimi, P., Paluszny, A., Pentland, C., 2013. Pore-scale imaging and modelling. *Adv. Water Resour.* 51, 197–216. <https://doi.org/10.1016/j.advwatres.2012.03.003>.
- Boon, M., Bijeljic, B., Niu, B., Krevor, S., 2016. Observations of 3-D transverse dispersion and dilution in natural consolidated rock by X-ray tomography. *Adv. Water Resour.* 96, 266–281. <https://doi.org/10.1016/j.advwatres.2016.07.020>.
- Boutchko, R., Rayz, V.L., Vandehey, N.T., O'Neil, J.P., Budinger, T.F., Nico, P.S., Druhan, J.L., Saloner, D.A., Gullberg, G.T., Moses, W.W., 2012. Imaging and modeling of flow in porous media using clinical nuclear emission tomography systems and computational fluid dynamics. *J. Appl. Geophys.* 76, 74–81. <https://doi.org/10.1016/j.jappgeo.2011.10.003>.
- Brattekas, B., Seright, R.S., 2017. Implications for improved polymer gel conformance control during low-salinity chase-floods in fractured carbonates. *J. Petrol. Sci. Eng.* <https://doi.org/10.1016/j.petrol.2017.10.033>. This.
- Brattekas, B., Steinsbo, M., Graue, A., Ferno, M., Espedal, H., Seright, R., 2016. New insight to wormhole formation in polymer gel during water chasefloods using positron emission tomography PET. *SPE 1–13*. 180051
- Brenner, D.J., Hall, E.J., 2007. Computed tomography an increasing source of radiation exposure. *N. Engl. J. Med.* 357 (22), 2277–2284. [https://doi.org/10.1016/s8756-3452\(08\)79173-4](https://doi.org/10.1016/s8756-3452(08)79173-4).
- Crandall, D., Moore, J., Gill, M., Stadelman, M., 2017. CT Scanning and flow measurements of shale fractures after multiple shearing events. *Int. J. Rock Mech. Min. Sci.* 100, 177–187. <https://doi.org/10.1016/j.ijrmms.2017.10.016>. October
- Defrise, M., Kinahan, P.E., Michel, C.J., 2003. Chapter 4: image reconstruction algorithms in PET. *Positron Emiss. Tomogr.* 63–91.
- Degueldre, C., Pleinert, H., Maguire, P., Lehman, E., Missimer, J., Hammer, J., Leenders, K., Böck, H., Townsend, D., 1996. Porosity and pathway determination in crystalline rock by positron emission tomography and neutron radiography. *Earth Planet. Sci. Lett.* 140 (1–4), 213–225. [https://doi.org/10.1016/0012-821X\(96\)00043-X](https://doi.org/10.1016/0012-821X(96)00043-X).
- Dogan, M., Moysey, S.M., Ramakers, R.M., DeVol, T.A., Beekman, F.J., Groen, H.C., Powell, B.A., 2017. High-resolution 4D pre-clinical SPECT/CT imaging of technetium transport within a heterogeneous porous media. *Environ. Sci. Technol.* <https://doi.org/10.1021/acs.est.6b04172>.
- Ferno, M., Gauteplass, J., Hauge, L.P., Abell, G.E., Adamsen, T.C.H., Graue, A., 2015. Combined positron emission tomography and computed tomography to visualize and quantify fluid flow in sedimentary rocks. *Water Resour. Res.* 51 (9), 7811–7819. <https://doi.org/10.1002/2015WR017130>. Received.
- Ferno, M.A., Hauge, L.P., Uno Rogmo, A., Gauteplass, J., Graue, A., 2015. Flow visualization of CO₂ in tight shale formations at reservoir conditions. *Geophys. Res. Lett.* 42 (18), 7414–7419. <https://doi.org/10.1002/2015GL065100>.
- Goethals, P., Volckaert, A., Jacobs, P., Roels, S., Carmeliet, J., 2009. Comparison of positron emission tomography and X-ray radiography for studies of physical processes in sandstone. *Eng. Geol.* 103 (3–4), 134–138. <https://doi.org/10.1016/j.enggeo.2008.06.015>.
- Gonzalez, R.C., Woods, R.E., 2017. *Digital Image Processing*, 4th ed. Pearson.
- Gouze, P., Tenchine, S., Loggia, D., Bruderer, C., Fedorov, A., Adler, P.M., Thovert, J.-F., Greswell, R., Riley, M., Parker, D.J., 2003. A study of the dispersion in a single thin fracture using positron emission projected imaging. *Groundwater Fractured Rocks* 407–408.
- Gründig, M., Richter, M., Seese, A., Sabri, O., 2007. Tomographic radiotracer studies of the spatial distribution of heterogeneous geochemical transport processes. *Appl. Geochem.* 22 (11), 2334–2343. <https://doi.org/10.1016/j.apgeochem.2007.04.024>.
- Hoff, W.D., Wilson, M.A., Benton, D.M., Hawkesworth, M.R., Parker, D.J., Flowles, P., 1996. The use of positron emission tomography to monitor unsaturated water flow within porous construction materials. *J. Mater. Sci. Lett.* 15 (13), 1101–1104. <https://doi.org/10.1007/BF00539949>.
- Hu, Y., Armstrong, R.T., Hung, T.-t., Lee, B., Shikhov, I., Mostaghimi, P., 2017. Analysing flow in rocks by combined positron emission tomography and computed tomography imaging. *Soc. Core Anal.* 082, 1–9.
- Hudson, H.M., Larkin, R.S., 1994. Ordered subsets of projection data. *IEEE Trans. Med. Imaging* 13 (4), 601–609. <https://doi.org/10.1109/42.363108>.
- Huo, D., Benson, S.M., 2016. Experimental investigation of stress-Dependency of relative permeability in rock fractures. *Transp. Porous Media* 113 (3), 567–590. <https://doi.org/10.1007/s11242-016-0713-z>.
- Huo, D., Pini, R., Benson, S.M., 2016. A calibration-free approach for measuring fracture aperture distributions using X-ray computed tomography. *Geosphere* 12 (2), 558–571. <https://doi.org/10.1130/GES01175.1>.
- Ketcham, R.A., Slottke, D.T., Sharp, J.M., 2010. Three-dimensional measurement of fractures in heterogeneous materials using high-resolution X-ray computed tomography. *Geosphere* 6 (5), 499–514. <https://doi.org/10.1130/ges00552.1>.
- Khalili, a., Basu, a.J., Pietrzyk, U., 1998. Flow visualization in porous media via positron emission tomography. *Phys. Fluids* 10 (4), 1031. <https://doi.org/10.1063/1.869627>.
- Kinahan, P.E., Defrise, M., Clackdoyle, R., 2004. Chapter 20 - Analytic Image Reconstruction Methods. Academic Press, pp. 421–442. <https://doi.org/10.1016/b978-012744482-6.50023-5>.
- Koriabkina, A.O., De Jong, A.M., Hensen, E.J., Van Santen, R.A., 2005. Concentration and temperature dependence of the diffusivity of n-hexane in MFI-zeolites. *Microporous Mesoporous Mater.* 77 (2–3), 119–129. <https://doi.org/10.1016/j.micromeso.2004.08.025>.
- Kulenkampff, J., Gründig, M., Richter, M., Enzmann, F., 2008. Evaluation of positron-emission-tomography for visualisation of migration processes in geomaterials. *Phys. Chem. Earth.* 33 (14–16), 937–942. <https://doi.org/10.1016/j.pce.2008.05.005>.
- Kulenkampff, J., Gründig, M., Zakhnini, A., Gerasch, R., Lippmann-Pipke, J., 2015. Process tomography of diffusion, using PET, to evaluate anisotropy and heterogeneity. *Clay Miner* 50 (3), 369–375. <https://doi.org/10.1180/claymin.2015.050.3.09>.
- Kulenkampff, J., Gründig, M., Zakhnini, A., Lippmann-Pipke, J., 2016. Geoscientific process monitoring with positron emission tomography (geopet). *Solid Earth* 7 (4), 1217–1231. <https://doi.org/10.5194/se-7-1217-2016>.
- Kulenkampff, J., Sto, M., Gründig, M., Manse, A., Lippmann-pipke, J., Kersten, M., 2018. Time-lapse 3D imaging by positron emission tomography of cu mobilized in a soil column by the herbicide MCPA. *Sci. Rep.* 8 (7091), 1–9. <https://doi.org/10.1038/s41598-018-25413-9>.
- Kurotori, T., Zahasky, C., Benson, S.M., Pini, R., 2018. Three-Dimensional Imaging of Solute Transport in Reservoir Rocks by Positron Emission Tomography. In: *Proceedings of the 14th International Conference on Greenhouse Gas Control Technologies*. Melbourne, Australia, pp. 1–7.
- Kurotori, T., Zahasky, C., Hosseinzadeh, S.A., Shah, S., Benson, S.M., Pini, R., 2018. Measuring, imaging and modelling solute transport in a microporous limestone. *Chem. Eng. Sci. In Press*.
- Lee, J., Yoon, H., Kitanidis, P.K., Werth, C.J., Valocchi, A.J., 2016. Scalable subsurface inverse modeling of huge data sets with an application to tracer concentration breakthrough data from magnetic resonance imaging. *Water Resour. Res.* 52, 1–20. <https://doi.org/10.1002/2014WR015716>.
- Levin, C.S., 2005. Primer on molecular imaging technology. *Eur. J. Nucl. Med. Mol. Imaging* 32 (SUPPL. 2). <https://doi.org/10.1007/s00259-005-1973-y>.
- Levin, C.S., Hoffman, E.J., 1999. Calculation of positron range and its effect on the fundamental limit of positron emission tomography system spatial resolution. *Phys. Med. Biol.* 44 (3), 781–799. <https://doi.org/10.1088/0031-9155/45/2/501>.
- Lippmann-Pipke, J., Gerasch, R., Schikora, J., Kulenkampff, J., 2017. Benchmarking PET for geoscientific applications: 3D quantitative diffusion coefficient determination in clay rock. *Comput. Geosci.* 101, 21–27. <https://doi.org/10.1016/j.jageo.2017.01.002>.
- Loggia, D., Gouze, P., Greswell, R., Parker, D.J., 2004. Investigation of the geometrical dispersion regime in a single fracture using positron emission projection imaging. *Transp. Porous Media* 55 (1), 1–20. <https://doi.org/10.1023/B:TIPM.0000007317.15987.95>.
- Maguire, R.P., Missimer, J.H., Emert, F., Townsend, D.W., Dollinger, H., Leenders, K.L., 1997. Positron emission tomography of large rock samples using a multiring PET instrument. *IEEE Trans. Nucl. Sci.* 44 (1), 26–30. <https://doi.org/10.1109/23.554819>.
- Maucec, M., Dusterhoft, R., Rickman, R., Gibson, R., Buffler, A., Heerden, M.V., 2013. Imaging of fluid mobility in fractured cores using time-lapse positron emission tomography. *SPE 1–12*. 166402
- Mitchell, J., Chandrasekera, T.C., Holland, D.J., Gladden, L.F., Fordham, E.J., 2013. Magnetic resonance imaging in laboratory petrophysical core analysis. *Phys. Rep.* 526 (3), 165–225. <https://doi.org/10.1016/j.physrep.2013.01.003>.
- Moses, W., 2011. Fundamental limits of spatial resolution in PET. *Nuclear Inst. Methods Phys. Res. Sect. A* 648, 1–14. <https://doi.org/10.1016/j.nima.2010.11.092>. Fundamental.
- Nestle, N., Baumann, T., Wunderlich, A., Niessner, R., 2003. MRI Observation of heavy metal transport in aquifer matrices down to sub-mg quantities. *Magn. Reson. Imaging* 21 (3–4), 345–349. [https://doi.org/10.1016/S0730-725X\(03\)00166-8](https://doi.org/10.1016/S0730-725X(03)00166-8).
- Niu, B., Al-Menhali, A., Krevor, S.C., 2015. The impact of reservoir conditions on the residual trapping of carbon dioxide in Berea sandstone. *Water Resour. Res.* 51, 1–21. [https://doi.org/10.1016/0022-1694\(68\)90080-2](https://doi.org/10.1016/0022-1694(68)90080-2).
- Noordhoek, N.J., van IJendoorn, L.J., Anderson, B.G., de Gauw, F.J., van Santen, R.A., de Voigt, M.J., 1998. Mass transfer of alkanes in zeolite packed-Bed reactors studied with positron emission profiling. 2. modeling. *Ind. Eng. Chem. Res.* 37 (3), 825–833. <https://doi.org/10.1021/ie970347j>.
- Ogilvie, S.R., Orribo, J.M., Glover, P.W.J., 2001. The influence of deformation bands upon fluid flow using profile permeametry and positron emission tomography. *Geophys. Res. Lett.* 28 (1), 61–64. <https://doi.org/10.1029/2000GL008507>.
- Perret, J., Prasher, S., Kantzas, A., Hamilton, K., Langford, C., 2000. Preferential solute flow in intact soil columns measured by SPECT scanning. *Soil Sci. Soc. Am. J.* 64 (2), 469–477. <https://doi.org/10.2136/sssaj2000.642469x>.
- Perrin, J.C., Benson, S., 2010. An experimental study on the influence of sub-core scale heterogeneities on CO₂ distribution in reservoir rocks. *Transp. Porous Media* 82 (1), 93–109. <https://doi.org/10.1007/s11242-009-9426-x>.
- Pini, R., Krevor, S.C., Benson, S.M., 2012. Capillary pressure and heterogeneity for the CO₂/water system in sandstone rocks at reservoir conditions. *Adv. Water Resour.* 38, 48–59. <https://doi.org/10.1016/j.advwatres.2011.12.007>.
- Pini, R., Vandehey, N.T., Druhan, J., Neil, J.P.O., 2016. Quantifying solute spreading and mixing in reservoir rocks using 3D PET imaging. *J. Fluid Mech* 796, 558–587. <https://doi.org/10.1017/jfm.2016.262>.
- Pinoli, J.-C., 2014. Key Concepts and Notions for IPA. In: *Mathematical Foundations of Image Processing and Analysis 1*, 1. Wiley-ISTE, pp. 39–45. <https://doi.org/10.1002/9781118625705.ch5>.
- Reeves, A., Chudek, J., 2001. Nuclear magnetic resonance imaging (MRI) of diesel oil migration in estuarine sediment samples. *J. Ind. Microbiol. Biotechnol.* 26 (1–2), 77–82.
- Richter, M., 2007. Concepts for Modelling of Heterogeneous Flow Processes in Soil Columns on the Basis of Tomographic Radiotracer Experiments. John Wiley & Sons, Ltd, pp. 20–38.
- Rose, A., 1974. *The Visual Process*. In: *Vision Human and Electronic*. Plenum Press, New York-London, pp. 1–27. <https://doi.org/10.1016/B978-1-4832-3089-4.50032-7>.
- Schumacher, R.R., Anderson, B.G., Noordhoek, N.J., Gauw, F.J.M.M.D., Jong, A.M.D., Voigt, M.J.A.D., Santen, R.A.V., 2000. Tracer-exchange experiments with positron emission profiling: diffusion in zeolites. *Microporous. Mesoporous. Mater.* 36, 315–326.

- Smith, S.L., Boothman, C., Williams, H.A., Ellis, B.L., Wragg, J., West, J.M., Lloyd, J.R., 2017. Microbial impacts on ^{99m}Tc migration through sandstone under highly alkaline conditions relevant to radioactive waste disposal. *Sci. Total Environ.* 575, 485–495.
- Thorpe, C.L., Williams, H.A., Boothman, C., Lloyd, J.R., 2019. Positron emission tomography to visualise in-situ microbial metabolism in natural sediments. *Appl. Radiat. Isot.* 144. <https://doi.org/10.1016/j.apradiso.2018.11.005>.
- Vandehey, N.T., Boutchko, R., Druhan, J.L., O'Neil, J.P., Nico, P.S., Slowey, A.J., Moses, W.W., 2013. Performance evaluation of SPECT imaging system for sediment column imaging. *IEEE Trans. Nucl. Sci.* 60 (2), 763–767. <https://doi.org/10.1109/TNS.2012.2232679>.
- Vandehey, N.T., Oneil, J.P., Slowey, A.J., Boutchko, R., Druhan, J.L., Moses, W.W., Nico, P.S., 2012. Monitoring TC dynamics in a bioreduced sediment: an investigation with gamma camera imaging of ^{99m}Tc -pertechnetate and ^{99m}Tc -DTPA. *Environ. Sci. Technol.* 46 (22), 12583–12590. <https://doi.org/10.1021/es302313h>.
- Vasco, D.W., Pride, S.R., Zahasky, C., Benson, S.M., 2018. Calculating trajectories associated with solute transport in a heterogeneous medium. *Water Resour. Res.* 54 (9), 6890–6908. <https://doi.org/10.1029/GRL2012-865>.
- Vogler, D., Ostvar, S., Paustian, R., Wood, B.D., 2018. A hierarchy of models for simulating experimental results from a 3D heterogeneous porous medium. *Adv. Water Resour.* 114, 149–163. <https://doi.org/10.1016/j.advwatres.2018.02.009>.
- Watanabe, N., Ishibashi, T., Ohsaki, Y., Tsuchiya, Y., Tamagawa, T., Hirano, N., Okabe, H., Tsuchiya, N., 2011. X-Ray CT based numerical analysis of fracture flow for core samples under various confining pressures. *Eng. Geol.* 123 (4), 338–346. <https://doi.org/10.1016/j.enggeo.2011.09.010>.
- Wenning Q. 2018. Investigating Petrophysical Properties of Reservoir Rocks Using Traditional and Computerized Tomography Techniques, PhD thesis, ETH Zurich, doi:10.3929/ethz-b-000304825.
- Wernick, M.N., Aarsvold, J.N., 2004. Introduction to emission tomography. In: Wernick, M.N., Aarsvold, J.N. (Eds.), *Emission Tomography: The Fundamentals of PET and SPECT*. Elsevier, pp. 11–23.
- Werth, C.J., Zhang, C., Brusseau, M.L., Oostrom, M., Baumann, T., 2010. A review of non-invasive imaging methods and applications in contaminant hydrogeology research. *J. Contam. Hydrol.* 113 (1–4), 1–24. <https://doi.org/10.1016/j.jconhyd.2010.01.001>.
- Zahasky, C., 2018. Advancing Utilization of Positron Emission Tomography for Quantifying Fluid Transport and CO₂ Trapping in Geologic Porous Media. Stanford University.
- Zahasky, C., Benson, S.M., 2016. Phase saturation validation and tracer transport quantification using micropet in a heterogeneous sandstone core. *Soc. Core Anal.* 1–12.
- Zahasky, C., Benson, S.M., 2018. Micro-Positron emission tomography for measuring sub-core scale single and multiphase transport parameters in porous media. *Adv. Water Resour.* 115, 1–16. <https://doi.org/10.1016/j.advwatres.2018.03.002>.
- Zahasky, C., Thomas, D., Matter, J., Maher, K., Benson, S.M., 2018. Multimodal imaging and stochastic percolation simulation for improved quantification of effective porosity and surface area in vesicular basalt. *Adv. Water Resour.* 121 (June), 235–244. <https://doi.org/10.1016/j.advwatres.2018.08.009>.
- Zakhnini, A., Kulenkampff, J., Sauerzapf, S., Pietrzyk, U., Lippmann-Pipke, J., 2013. Monte carlo simulations of geopot experiments: 3D images of tracer distributions (18f,124i and 58co) in opalinus clay, anhydrite and quartz. *Comput. Geosci.* 57, 183–196. <https://doi.org/10.1016/j.cageo.2013.03.023>.